Available online at www.sciencedirect.com
ScienceDirect
Journal of Computational Physics 227 (2008) 5871–5895
JOURNAL OF COMPUTATIONAL PHYSICS
www.elsevier.com/locate/jcp

Evaporation model for interfacial flows based on a continuum-field representation of the source terms

S. Hardt [a,*], F. Wondra [b]

[a] Institut für Nano- und Mikroprozesstechnik, Leibniz Universität Hannover, Callinstraße 36, 30167 Hannover, Germany
[b] Fachgebiet Technische Thermodynamik, TU Darmstadt, Petersenstraße 30, 64287 Darmstadt, Germany

Received 4 January 2007; received in revised form 13 February 2008; accepted 19 February 2008
Available online 29 February 2008

Abstract

An evaporation model compatible with interface-capturing schemes for vapor–liquid flow is presented. The model formulation is largely independent of the specific realization of interface-capturing and relies on a continuum-field representation of the source terms implementable in a broad class of CFD models. In contrast to most other numerical methods for evaporating interfacial flows, the model incorporates an evaporation source-term derived from a physical relationship for the evaporation mass flux. It is shown that especially for microscale evaporation phenomena this implies significant deviations of the interface temperature from the saturation temperature. The mass source-term distribution is derived from the solution of an inhomogeneous Helmholtz equation that contains a free parameter allowing to tune the spatial localization of the source. The evaporation model is implemented into the volume-of-fluid scheme with piecewise linear interface construction. Results are obtained for three analytically or semi-analytically solvable model problems, the first two being one-dimensional Stefan problems, the third a free droplet evaporation problem. In addition, a two-dimensional film boiling problem is considered. Overall, the comparison between the CFD and the (semi)-analytical models shows good agreement. Deviations exist where convective heat transfer due to spurious currents is no longer negligible compared to heat conduction. With regard to the film boiling problem, a similar evaporation pattern as recently identified using a level-set method is found. A major advantage of the developed evaporation model is that it does not refer to intrinsic details of the interface-capturing scheme, but relies on continuum-field quantities that can be computed by virtually any CFD approach.

Keywords: Evaporation model; Interfacial flow; Volume-of-fluid method; Stefan problem; Droplet evaporation; Film boiling

1. Introduction

In the past decades a variety of computational schemes for the computation of free-surface or interfacial flows have been developed. There are mainly two classes of approaches to model such types of flows. The first class contains the interface-tracking methods where a boundary-fitted grid is used to follow the motion of a vapor–liquid or liquid–liquid interface. This implies that the grid has to deform to follow to interfacial motion.

* Corresponding author. Tel.: +49 511 7622278.
E-mail address: hardt@nmp.uni-hannover.de (S. Hardt).

0021-9991/$ - see front matter © 2008 Elsevier Inc. All rights reserved.
doi:10.1016/j.jcp.2008.02.020

The second class contains the interface-capturing methods that rely on a fixed grid on which a numerical representation of the interface is propagated. Interface-tracking methods potentially provide a high-level of accuracy but are usually limited to specific types of problems and are not easily capable of modeling topologically nontrivial scenarios such as droplet pinch-off or coalescence. By contrast, interface-capturing methods have proven to be versatile and powerful schemes for computation of a broad class of flows and therefore have found much more widespread use than interface-tracking schemes. For this reason they form the fundament of the work reported in this article.

Two of the most popular versions of interface-tracking methods are the volume-of-fluid (VOF) [10] and the level-set [16] scheme. In the VOF method a scalar field quantity is introduced and advected on the grid encoding the volume-fraction of the two fluid phases. The fluid interface is located where the volume-fraction function shows a sharp transition between the two values representing the two different phases. The level-set approach is similar to the VOF scheme in the sense that a scalar field quantity – the level-set function – signaling the presence of either one of the two phases is advected on a grid. However, in this case the field quantity is not interpreted as a fluid volume fraction, but as a distance to the interface which itself corresponds to an isovalue manifold of the level-set function. An alternative interface-capturing scheme was developed in the group of Tryggvason [25]. In this so-called front-tracking scheme the fluid interface is represented by marker points connected by line segments. Interface advection is done by moving the marker points on a fixed grid.

In the past decade interface-tracking schemes have been extended to account for evaporative mass transfer between the phases. Corresponding extensions of the numerical models have been reported for the level-set [20,21,1,28,14,7,23], the VOF [27] and the front-tracking scheme [12,29], as well as for a combined level-set-VOF method [24]. While it has been convincingly demonstrated in many cases that using these approaches evaporating interfacial flows can be modeled accurately, the schemes referred to above are usually quite specific. Here the term "specific" refers to the fact that often quite limiting assumptions about the boundary conditions at the fluidic interface are made or that the implementation of evaporative mass transfer is done by referring to special, intrinsic details of the numerical schemes. As far as the thermal boundary condition at the fluidic interface is concerned, it is almost standard to assume that the interface is at saturation temperature [20,21,1,14,7,23,27,29,24]. This, however, is a simplifying assumption that can be violated in specific cases, as discussed in detail by Juric and Tryggvason [12]. The implementation of evaporative mass transfer has been done by deriving a source-term distribution from a special "smeared-out" heaviside function [20,21,1,14], by introducing a mass-correction step in the numerical calculation of the level-set function [28], by adding a mass source-term to the cells that are cut by the fluid interface [27,24], or by iteratively determining the velocity of the interface markers taking into account the mass source-term [12].

By contrast, in this article a numerical evaporation model is presented that does not refer to details of the specific numerical algorithms used for solving the continuity, momentum, phase distribution and enthalpy equations and that should be applicable in the context of both the VOF and the level-set scheme. All quantities needed for implementing the effects of phase change are derived from scalar fields computed on a numerical grid. The method is constructed in such a way that the phase change feature can be added to an existing interface-tracking algorithm the numerical details of which (grid type, type of discretization, etc.) are largely unimportant. In addition, the method allows accommodation of a broad class of boundary conditions at the fluid interface and is not limited to a situation where the interface is at a fixed temperature.

2. Thermal boundary condition at the vapor–liquid interface

Before turning to the actual evaporation model, it is helpful to spend a few thoughts on the thermal boundary condition at the vapor–liquid interface. This is especially true since in CFD models for evaporating flows the interface temperature is almost always set equal to the saturation temperature, whereas a claim of the method to be developed in this article is to allow a simple incorporation of more general relationships.

The question in which specific situations significant deviations of the interface temperature from the saturation value may occur can in principle be answered by referring to the detailed analysis of Juric and Tryggvason [12]. Here, this problem should be revisited in a somewhat simplified context. One of the simplest models accounting for deviations of the interfacial temperature from the saturation temperature is that of Tanasawa [22] which contains a linear dependence of the heat flux on the excess temperature of the phase boundary:

$$j_e^h = \alpha_e(T_i - T_{sat}), \tag{1}$$

where j_e^h is the evaporation heat flux density, T_i the temperature of the phase boundary, and T_{sat} the saturation temperature. The evaporation heat transfer coefficient is given by

$$\alpha_e = \frac{2\chi_e}{2-\chi_e}\frac{h_e^2}{\sqrt{2\pi R}}\frac{\rho_v}{T_{sat}^{3/2}}, \tag{2}$$

where χ_e is the evaporation coefficient, h_e the enthalpy of evaporation, R the gas constant for water and ρ_v the vapor density. In order to quantify the deviations of the interfacial temperature from the saturation temperature, the situation sketched in the inset of Fig. 1 is considered. A vapor–liquid interface is located at a distance d from a solid wall at constant temperature $T_0 > T_i$. Using

$$j^h = j_e^h = \lambda\frac{T_0 - T_i}{d}, \tag{3}$$

where j^h is the heat flux from the wall to the interface and λ the thermal conductivity, one finds the dimensionless deviation of the interfacial temperature from the saturation temperature:

$$\frac{T_i - T_{sat}}{T_0 - T_{sat}} = \frac{1}{1+\frac{\alpha_e d}{\lambda}}. \tag{4}$$

This function of the dimensionless parameter $x = \alpha_e d/\lambda$ is displayed in Fig. 1. The deviation of the interfacial temperature from the saturation temperature is increasing with decreasing length scale d. This means that especially when studying evaporation phenomena on the micro- and nanoscale it has to be taken into account that the temperature of a vapor–liquid interface is not necessarily equal to the saturation temperature. Taking the evaporation of water at atmospheric pressure as an example and assuming an evaporation coefficient of 0.1, at a length scale of $d \approx 81$ μm the dimensionless temperature deviation is equal to 0.01, while at $d \approx 7$ μm it has increased to 0.1. This simple example shows that on small length scales the deviations of the interfacial temperature from the saturation temperature can no longer be neglected.

It should be emphasized that heat and mass transfer through vapor–liquid interfaces are complex phenomena for which a number of effects not included in Eq. (2) may play a role. The importance and interplay of these effects are discussed in a review article by Wayner [26]. A curved interface causes a Laplace pressure that can lead to local deviations from the equilibrium with the vapor phase at saturation pressure. Van der Waals forces between the solid wall and the liquid equally shift the equilibrium between the two phases and may give rise to a thin adsorbed liquid film. In an electrolyte, a Debye layer can form at a solid wall, making it necessary

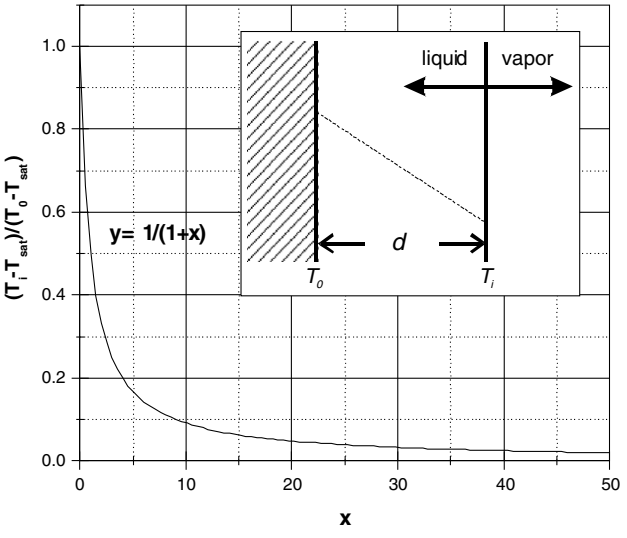

Fig. 1. Dimensionless deviation of the interfacial temperature as a function of $x = \alpha_e \cdot d/\lambda$. The inset shows the situation considered.

to include electrostatic forces in the analysis that cause a further shift of the phase equilibrium. The latter two phenomena, van der Waals and electrostatic forces, usually become important for liquid films with a thickness of some 10 nm. The aim of the present work is not to build a model for the variety of these phenomena, but to provide a framework for the simple implementation of suitable evaporation models.

The numerical scheme to be presented in the following chapters has been developed especially to study micro- and sub-microscale evaporation phenomena, but is not limited to this regime. It also allows incorporation of a number of different evaporation models, given that the temperature jump across the vapor–liquid interface can be neglected. Bond and Struchtrup [3] provide a detailed analysis of the different results and limiting cases of kinetic gas theory for the evaporation mass flux. Key quantities of these models are the interaction parameters of vapor molecules with a vapor–liquid interface. The condensation coefficient is the probability that a molecule hitting the liquid surface gets adsorbed. Analogously, the evaporation coefficient measures how many molecules escape from the surface. The classical evaporation theories of Hertz–Knudsen [9,13] and Schrage [19] incorporate certain assumptions for the condensation and evaporation coefficients, besides relying on specific relationships between these coefficients. In Hertz–Knudsen theory the condensation coefficient is equal to 1, whereas in Schrage's theory a condensation coefficient independent of the molecular impact energy is assumed. In principle, after the decision about the fluid system to consider has been made, the choice of the specific evaporation model can be based on corresponding experimental data for the condensation and evaporation coefficients and their energy dependence. Throughout this work the model of Eqs. (1) and (2) will be used that incorporates a linear relationship between the evaporation heat or mass flux and the temperature difference at the interface. Such a linear relationship can be derived from Schrage's theory in the case of small deviations from equilibrium, i.e. $(T_i - T_{\mathrm{sat}})/T_{\mathrm{sat}} \ll 1$ [22].

3. Governing equations and numerical model

In this section the underlying equations for transport of mass, momentum and heat are defined and it is shown how evaporative mass transfer between the two phases can be incorporated using an additional scalar field. Furthermore, it is assumed that the distribution of vapor and liquid is computed based on the level-set, the VOF, or a similar scheme. The numerical model is largely independent of the specific interface-tracking scheme. Therefore, in this section only a few basic assumptions about the way of computing the phase distribution are made.

Both fluids are treated as incompressible, so that the momentum conservation equation is given by

$$\rho\left(\frac{\partial \mathbf{u}}{\partial t} + (\mathbf{u}\cdot\nabla)\mathbf{u}\right) = -\nabla p + \nabla\cdot\boldsymbol{\tau} + \sigma\kappa\nabla C + \mathbf{f}, \tag{5}$$

where the viscous stress tensor is defined by

$$\tau_{ij} = \mu\left(\frac{\partial u_i}{\partial x_j} + \frac{\partial u_j}{\partial x_i}\right). \tag{6}$$

The velocity and pressure fields are denoted as $\mathbf{u}$ and p, respectively, the density ρ and viscosity μ are position-dependent quantities, assuming values of ρ_l, μ_l in the liquid and ρ_{v}, μ_{v} in the vapor phase, while the surface tension σ is assumed to be constant. C denotes the liquid volume-fraction. It is assumed that there exists a sharp interface between vapor and liquid, so C either assumes a value of 1 or 0. Correspondingly, the vapor volume-fraction is given as $1 - C$. κ is the curvature of the interface, expressed as

$$\kappa = -\nabla\cdot\frac{\nabla C}{|\nabla C|}. \tag{7}$$

All body forces such as gravity are collected in $\mathbf{f}$. The mass conservation equation is written as

$$\rho\nabla\cdot\mathbf{u} = \dot{\rho}, \tag{8}$$

where the meaning and form of the source-term $\dot{\rho}$ will be explained below. The enthalpy equation is

$$\frac{\partial}{\partial t}(\rho c_p T) + \nabla\cdot(\rho c_p \mathbf{u} T) = \nabla\cdot(\lambda\nabla T) + \dot{h}, \tag{9}$$

where T denotes temperature and the material properties, c_p (specific heat capacity at constant pressure) and λ (thermal conductivity) assume values c_{pl}, λ_l in the liquid and c_{pv}, λ_v in the vapor phase. $\dot{h}$ is a source-term that may contain contributions from physical heat sources in addition to model-specific terms, which will be detailed below. Contributions from viscous heating are neglected in Eq. (9).

The essence of the evaporation model lies in the choice of the source terms, especially in their spatial distribution. $\dot{\rho}$ will be chosen such that on the liquid side of a vapor–liquid interface, mass disappears and reappears on the vapor side. $\dot{h}$ will contain the contribution of the enthalpy of evaporation, among others. As a first step, the gradient of the volume-fraction field is computed:

$$C' = |\nabla C| . \tag{10}$$

The volume-fraction appears as a primary field quantity within the VOF method. Within the level-set method, C is computed via

$$C = \theta(\zeta), \tag{11}$$

where θ is the heaviside and ζ the level-set function. An important feature of C' is that its integral over a region enclosing a part of the vapor–liquid interface measures the interface content:

$$\int_\Omega |\nabla C| \, d\Omega = \int_S dS, \tag{12}$$

as sketched in Fig. 2. Thus, in three spatial dimensions the volume integral gives the interface area, in two dimensions the corresponding area integral gives the interface length.

As a next step, the physical model for evaporative mass transfer has to be implemented. The evaporation model is introduced as an evaporation mass flux $j_e(T_i, T_{sat})$ (in units mass per time per area), where T_i is the interface temperature and T_{sat} is the saturation temperature corresponding to the pressure on the liquid side of the interface. T_{sat} may deviate from the corresponding saturation temperature in the vapor phase since the interface curvature may cause a pressure jump. Both T_i and T_{sat} are quantities that depend on the solution field of the flow simulation. They should be determined in each time step of a numerical computation. To sample the local evaporation rate, the field

$$\varphi_0 = N j_e C C' \tag{13}$$

is computed. N is a normalization factor to be determined from the equation

$$N \int_\Omega CC' d\Omega = \int_\Omega C' d\Omega, \tag{14}$$

where Ω is the domain for the flow computation. In Eq. (13) the factor C is introduced to ensure that only field values on the liquid side of the interface determine the evaporation mass flux. Using Eqs. (14) and (12) it is easy to show that the choice $\dot{\rho} = -\varphi_0$ yields the correct rate of disappearance of liquid through the interface based on the evaporation model $j_e(T_i, T_{sat})$. Yet it has to be made sure that the same mass reappears on the vapor side of the interface.

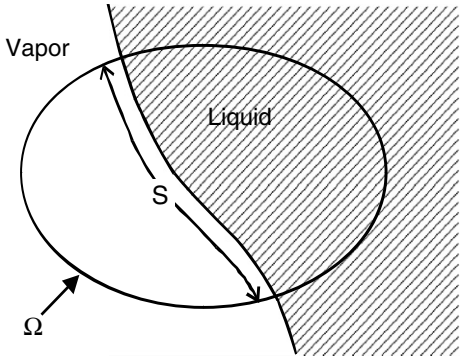

Fig. 2. Visualization of the integration regions of Eq. (12).

In principle, evaporative mass transfer could be implemented into an interface-capturing model by introducing the source-term of Eq. (13) and a corresponding counterpart on the vapor side into the mass conservation equation. This, however, results in a source-term distribution localized in a very narrow region at the interface which was found to lead to numerical instabilities, as will be discussed later. To avoid instabilities, a source-term distribution smeared-out over a few computational cells in the vicinity of the interface is needed. A more suitable distribution can be computed by solving an inhomogeneous Helmholtz equation for an additional scalar field φ:

$$\nabla^2\varphi = \frac{1}{\Delta t D}(\varphi - \varphi_0), \tag{15}$$

where Δt is a parameter with dimension of time and D a diffusion constant. This equation has to be solved in the entire computational domain for the flow problem Ω, for each time step of a transient simulation, and with the boundary condition

$$\mathbf{n}\cdot\nabla\varphi|_{\partial\Omega} = 0, \tag{16}$$

where $\mathbf{n}$ is a unit normal vector on the boundary. Via Gauss's theorem

$$\frac{1}{\Delta t D}\int_\Omega(\varphi-\varphi_0)\mathrm{d}\Omega = \int_\Omega\nabla^2\varphi\mathrm{d}\Omega = \int_{\partial\Omega}(\nabla\varphi)\cdot\mathrm{d}\mathbf{S} = 0, \tag{17}$$

this boundary condition ensures that the volume integrals of φ and φ_0 are identical. To understand why φ is a smeared-out version of φ_0 and how the parameter combination $\Delta t D$ controls the degree of smearing, consider a time-dependent "concentration" field ψ with the identification

$$\psi(t)\equiv\varphi_0, \quad \psi(t+\Delta t)\equiv\varphi. \tag{18}$$

Then Eq. (15) can be rewritten as

$$\psi(t+\Delta t) = \psi(t) + \Delta t D\nabla^2\psi(t+\Delta t) \tag{19}$$

which is an implicit first-order time stepping scheme for solving the diffusion equation

$$\frac{\partial\psi}{\partial t} = D\nabla^2\psi. \tag{20}$$

Thus, φ approximates a diffusively smeared version of φ_0 with Δt being the time increment between the original and the smeared distribution and D the corresponding diffusion constant. The length scale over which the original source-term is smeared is given by $(\Delta t D)^{1/2}$. From φ the complete source-term incorporating evaporative mass transfer between the phases is determined as

$$\dot\rho = N_\mathrm{v}(1-C)\varphi - N_l C\varphi. \tag{21}$$

The first term accounts for creation of mass on the vapor side, the second term for disappearance of mass on the liquid side of the interface. The normalization factors N_v and N_l ensure that all mass that disappears reappears on the other side of the interface and that the evaporation mass flux density assumes the correct value $j_\mathrm{e}(T_i, T_\mathrm{sat})$. They are determined from the equations

$$\begin{aligned} N_\mathrm{v}\int_\Omega(1-C)\varphi\mathrm{d}\Omega &= \int_\Omega\varphi\mathrm{d}\Omega \\ N_l\int_\Omega C\varphi\mathrm{d}\Omega &= \int_\Omega\varphi\mathrm{d}\Omega \end{aligned} \tag{22}$$

The source-term $\dot h$ in the enthalpy equation contains a contribution from the enthalpy of evaporation, i.e. a cooling term reflecting the latent heat of the phase change which has to be coupled to the mass source-term. Before addressing this contribution, another aspect should be examined. Owing to the structure of the mass source term of Eq. (21), there is a finite region around the vapor–liquid interface over which liquid disappears and vapor emerges, referred to as the evaporation region. This situation is sketched in Fig. 3 in which the convective enthalpy flux density $j^\mathrm{h} = \rho c_p u_n T$ is schematically plotted along a direction x normal to the interface in a coordinate frame co-moving with the interface. u_n is the velocity component normal to the interface and it

$$\dot{h}_c = \left(N_v(1-C)c_{pv} - N_l C c_{pl}\right)T\varphi.$$

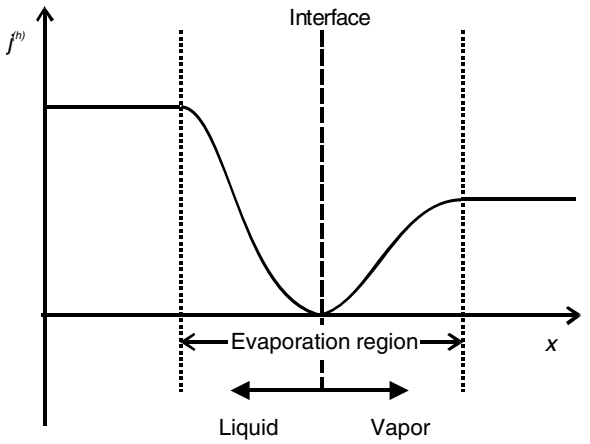

Fig. 3. Sketch of the convective enthalpy flux across the vapor–liquid interface for constant temperature.

has been assumed that T does not vary significantly in the x-range considered. On the liquid side of the interface, the enthalpy flux decreases due to the decreasing mass flux. The opposite effect is observed on the vapor side. However, bearing in mind that Eq. (9) is a conservation equation, such a collapse of the enthalpy flux as sketched in Fig. 3 cannot happen. Rather than that, the coupled solution of the momentum and enthalpy equations together with the mass conservation results in a heating of liquid and a cooling of vapor in the evaporation region, generating a temperature peak at the interface. This is an artifact of the structure of the mass source-term and has to be removed. It can be removed by adding a correction source-term

$$\dot{h}_c = (N_v(1-C)c_{pv} - N_l C c_{pl})T\varphi. \tag{23}$$

As far as the source-term from the enthalpy of evaporation is concerned, the numerical experiments reported in the following sections have indicated that it is not necessary to compute a smeared version as in the case of the mass source-term. An enthalpy source-term localized in a narrow region around the interface does not seem to cause any numerical problems. Therefore, the cooling due to evaporation is accounted for by a term

$$\dot{h}_e^{(1)} = -h_e\varphi_0. \tag{24}$$

Alternatively, the source-term can also be shifted to the liquid side of the interface

$$\dot{h}_e^{(2)} = -h_e N_l^{(0)} C\varphi_0, \tag{25}$$

or to the vapor side

$$\dot{h}_e^{(3)} = -h_e N_v^{(0)}(1-C)\varphi_0, \tag{26}$$

where the normalization factors are determined from

$$\begin{aligned} N_v^{(0)} \int_\Omega (1-C)\varphi_0 \mathrm{d}\Omega &= \int_\Omega \varphi_0 \mathrm{d}\Omega \\ N_l^{(0)} \int_\Omega C\varphi_0 \mathrm{d}\Omega &= \int_\Omega \varphi_0 \mathrm{d}\Omega \end{aligned} \tag{27}$$

It should be noted that the difference between Eqs. (24)–(26) only exists on a finite grid and vanishes in the limit of zero grid spacing, since then φ_0 becomes proportional to a delta function located at the interface. Finally, the complete source-term for Eq. (9) is given as a sum of three different contributions

$$\dot{h} = \dot{h}_c + \dot{h}_e^{(i)} + \dot{h}', \tag{28}$$

where $\dot{h}_e^{(i)}$ refers to any of the three versions Eq. (24), (25), or (26) and $\dot{h}'$ contains all other source terms, e.g. from exo- or endothermic chemical reactions.

This completes the specification of the evaporation model. Again, it should be noted that this model is solely based on the continuum quantities C and φ and a priori does not refer to specific realizations of interface-tracking schemes such as the level-set or the VOF method. The accuracy of the model depends on a number of different factors. First of all, there are the usual numerical errors related to the methods for solving the mass, momentum, and enthalpy conservation equation as well as the interface-capturing scheme. These will not be further discussed here, since the evaporation model is largely independent of the specific choice of these schemes. Secondly, there is a generic error of the evaporation model that can be traced back to Eq. (15). The normalization factors N_g and N_l in Eq. (21) ensure global mass conservation, but the method for computing the mass source terms on both sides of the vapor–liquid interface can violate local mass conservation, thereby introducing a non-local coupling to the model. This effect can be understood from Fig. 4 that shows the field φ in the vicinity of a flat (solid line) and a curved (dotted line) interface as a function of the interface-normal coordinate x. For reasons of symmetry the integrals of φ in the vapor and the liquid phase are the same if the interface is flat, whereas a curved interface leads to a non-symmetric φ with one of the integrals being bigger than the other. Translated to the mass source terms this means that more liquid disappears than reappears as vapor on the other side or vice versa.

In order to compute the magnitude of the error related to curved interfaces, a spherical surface with radius b is considered as the prototype of a curved interface. For this sphere, two integrals are defined as

$$\Gamma_< = \int_0^b \varphi(r) r^2 \mathrm{d}r, \quad \Gamma_> = \int_b^\infty \varphi(r) r^2 \mathrm{d}r. \tag{29}$$

As a measure for the numerical error the asymmetry parameter

$$\delta = \frac{\Gamma_> - \Gamma_<}{\Gamma_> + \Gamma_<}. \tag{30}$$

is used. In Appendix A it is shown that

$$\delta \approx \frac{\sqrt{a}}{b} \tag{31}$$

to leading order in $a^{1/2}/b$, the length scale over which the smearing of the mass source-term is performed (with $a = \Delta t D$) divided by the radius of curvature. To suppress the violation of local mass conservation and the occurrence of non-local coupling terms, $a^{1/2}/b$ should be as small as possible. In practice, the length scale $a^{1/2}$ should extend over a few grid cells to avoid numerical instabilities. When the grid is refined, $a^{1/2}$ can be reduced proportionally, as becomes evident from the numerical experiments reported in the following

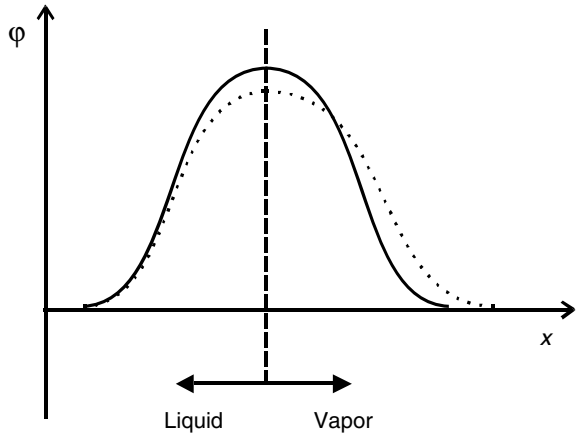

Fig. 4. Sketch of the scalar field from which the source-term distribution is derived in the case of a flat (solid line) and a curved (dotted line) interface.

sections. Thus, whenever the time evolution of curved interfaces is computed, the grid should be chosen fine enough to guarantee that $a^{1/2}/b$ always stays a small number, whereupon b is the local curvature of the interface.

4. Validation cases

In this section three analytically or semi-analytically solvable problems and one additional problem are presented which will serve as benchmark cases for the evaporation model. The first one is a one-dimensional test case where heat is transferred through a vapor phase to a vapor–liquid interface. The second one, also set up in one spatial dimension, concerns the evaporation of a liquid film. The third one is a spherically symmetric droplet evaporation problem. In addition, a film boiling problem is considered, for which, however, only numerical solutions are known.

4.1. Stefan problem 1

This problem has already been considered by Son and Dhir [20] and by Welch and Wilson [27]. Heat is transferred by conduction from a flat, isothermal surface through a vapor phase to a liquid (cf. Fig. 5). The surface is at a temperature above the saturation temperature, so liquid evaporates, leading to a motion of the interface to the right. It is assumed that during the evaporation process the interface stays flat. Therefore the problem can be regarded as one-dimensional.

The boundary conditions are

$$\begin{aligned} T(x=0,t) &= T_0 \\ T(x=x_i(t),t) &= T_{\text{sat}} \end{aligned} \tag{32}$$

The velocity u_i of the vapor–liquid interface is determined from

$$\rho_{\text{g}} h_{\text{e}} u_i = -\lambda_{\text{v}} \left.\frac{\partial T}{\partial x}\right|_{x=x_i-\varepsilon}, \tag{33}$$

where ε is an infinitesimal positive number. As an initial condition, $x_i\ (t=0)=0$ is assumed. The solution to this problem has been worked out long ago by Neumann and is given as [8]

$$\begin{aligned} x_i(t) &= 2\beta\sqrt{k_{\text{v}} t} \\ T(x,t) &= T_0 + \frac{T_{\text{sat}} - T_0}{\operatorname{erf}(\beta)} \operatorname{erf}\left(\frac{x}{2\sqrt{k_{\text{v}} t}}\right) \end{aligned} \tag{34}$$

where $k_{\text{v}} = (\lambda_{\text{v}})/(\rho_{\text{v}} c_{pv})$ is the thermal diffusivity, erf is the error function and β is determined from

$$\beta \exp(\beta^2)\operatorname{erf}(\beta) = \frac{c_{pv}(T_0 - T_{\text{sat}})}{\sqrt{\pi} h_{\text{e}}}. \tag{35}$$

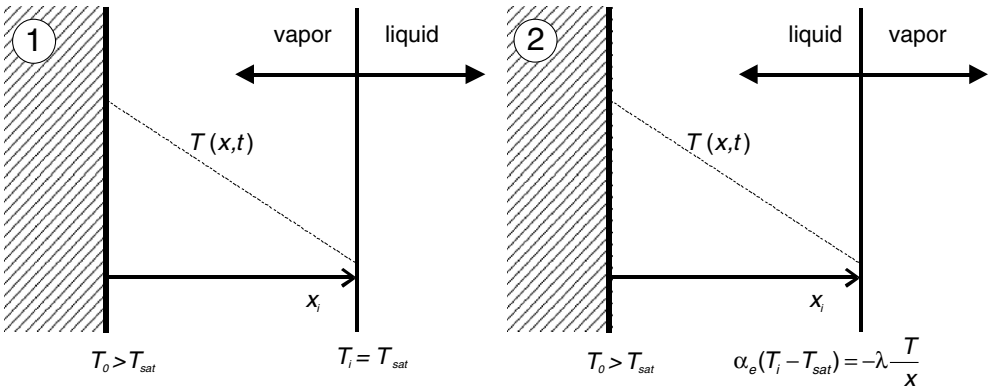

Fig. 5. Specification of the first (left) and the second (right) Stefan problem.

4.2. Stefan problem 2

The geometry and boundary conditions of this problem are depicted on the right side of Fig. 5. A liquid film covers a heated wall and evaporates. The wall surface is at a constant temperature above the saturation temperature, while this time the simple boundary condition of an isothermal vapor–liquid interface is replaced by

$$\alpha_e(T(x = x_i(t), t) - T_{sat}) = -\lambda_l \left.\frac{\partial T}{\partial x}\right|_{x=x_i-\varepsilon}. \tag{36}$$

In this expression, α_e is the evaporation heat transfer coefficient of Eq. (2) and ε is an infinitesimal positive number. Again, it is assumed that during the evaporation process the interface stays flat, so the problem can be regarded as one-dimensional.

The main purpose of considering this test case lies in the computation of the pressure drop originating from phase change. The incompressibility condition imposed in this work together with the density difference between the liquid and the vapor demands for an acceleration of the fluid when it changes its phase. The pressure drop required to drive this acceleration is known as *recoil pressure* and can easily be calculated analytically. Taking into account that, owing to the symmetry of the problem, there are no shear stresses and corresponding viscous pressure losses, the sum of potential and kinetic energy is constant across the interface, i.e.

$$p + \frac{\rho}{2}u^2\Big|_{x=x_i-\varepsilon} = p + \frac{\rho}{2}u^2\Big|_{x=x_i+\varepsilon}, \tag{37}$$

where p, ρ, u are pressure, density and flow velocity, respectively. In other words, the sum of the static pressure $p_{stat} = p$ and the dynamic pressure $p_{dyn} = \rho u^2/2$ assumes the same value on both sides of the interface.

In fact there is also a recoil pressure effect in the previously defined test case, Stefan problem 1. However, due to the large density difference between liquid and vapor the interface is heavily accelerated in this case whereas it moves only comparatively slowly in the case considered here. In Stefan problem 1, an analysis of the recoil pressure would have to include inertial forces in an accelerated reference frame. For this reason a second test case was set up that is more straightforward to analyze.

4.3. Droplet evaporation

As a third validation case, the evaporation of a spherical, uniformly heated droplet is considered (cf. Fig. 6). It is assumed that the spherical symmetry is not broken during the evaporation process which allows reducing the problem to a one-dimensional case. Analogously as in Eq. (36), at the vapor–liquid interface the heat flux is given as

$$\alpha_e(T(r = b(t), t) - T_{sat}) = -\lambda_l \left.\frac{\partial T}{\partial r}\right|_{r=b-\varepsilon}, \tag{38}$$

where α_e is the evaporation heat transfer coefficient of Eq. (2). The radial coordinate and the droplet radius are denoted as r and b, respectively. The temperature field inside the droplet is computed by solving the heat conduction equation subject to the boundary condition of Eq. (38).

The evaporation heat transfer goes along with an evaporation mass flux density of

$$j_e = \frac{1}{h_e}\alpha_e(T(r = b(t), t) - T_{sat}). \tag{39}$$

The time evolution of the droplet radius is obtained from mass conservation:

$$4\pi b^2 j_e = -\rho_l \frac{4\pi b^2 \mathrm{d}b}{\mathrm{d}t} \tag{40}$$

yielding

$$\frac{\mathrm{d}b}{\mathrm{d}t} = -\frac{j_e}{\rho_l}, \tag{41}$$

where j_e is a function of time via Eq. (39).

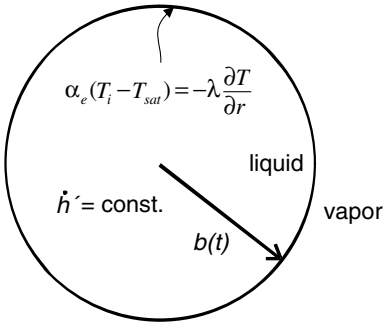

Fig. 6. Specification of the droplet evaporation problem.

The solution for the temperature field within the droplet can be obtained using the method of Green's functions. As described in [2], the general form of the temperature field $T = T - T_{\text{sat}}$ fulfilling the boundary condition Eq. (38) is

$$T(r,t) = \int_0^b G(r,t \mid r',0)\, T_0(r') 4\pi r'^2 \mathrm{d}r' + \frac{1}{\rho_l c_{pl}} \int_{t'=0}^{t} \int_{r'=0}^{b} G(r,t \mid r',t') \dot{h}'(r',t') 4\pi r'^2 \mathrm{d}r' \mathrm{d}t', \tag{42}$$

where $T_0(r)$ is the temperature distribution T over the sphere at $t = 0$ and $\dot{h}'(r,t)$ is the heating rate distribution. G is the Green's function for the sphere fulfilling the boundary condition Eq. (38), written as [2]

$$G(r,t \mid r',t') = \frac{1}{2\pi b r r'} \sum_{m=1}^{\infty} \exp\left(-\beta_m^2 \frac{k_l}{b^2}(t-t')\right) \frac{\beta_m^2 + B^2}{\beta_m^2 + B^2 + B} \sin\left(\beta_m \frac{r}{b}\right) \sin\left(\beta_m \frac{r'}{b}\right), \tag{43}$$

where $k_l = \lambda_l/(\rho_l c_{pl})$ and

$$\begin{aligned} B &= \frac{\alpha_e b}{\lambda} - 1 \\ \beta_m \cot \beta_m &= -B \end{aligned} \tag{44}$$

Here the case should be considered that $T_0(r) = 0$ and $\dot{h}'$ is space time independent. Then the integrations of Eq. (42) are easily performed, resulting in

$$T(r,t) = \frac{2\dot{h}' b^3}{\lambda_l} \sum_{m=1}^{\infty} \frac{1}{\beta_m^2} \left(1 - \exp\left(-\frac{k_l \beta_m^2}{b^2} t\right)\right) \frac{\beta_m^2 + B^2}{\beta_m^2 + B^2 + B} \left(\frac{\sin \beta_m}{\beta_m^2} - \frac{\cos \beta_m}{\beta_m}\right) \frac{\sin(\beta_m r/b)}{r}. \tag{45}$$

When inserting $T(r = b, t)$ into Eq. (39) and using the resulting expression in Eq. (41), a nonlinear ordinary differential equation in the unknown $b(t)$ is obtained. This can be solved by any standard integration scheme, yielding the radius of the evaporating droplet as a function of time and via Eq. (45) the time-dependent temperature profile.

4.4. Film boiling

Finally, a two-dimensional film boiling problem is considered. The situation studied is depicted in Fig. 7. A solid wall heated to a temperature above the saturation temperature of a liquid is covered by a thin vapor film above which the corresponding liquid phase is found. Because of the higher density of the liquid compared to vapor, a Rayleigh-Taylor instability is triggered, amplifying perturbations of the vapor–liquid interface and finally leading to the growth of bubbles. The most unstable wavelength is given by

$$\lambda_0 = 2\pi \sqrt{\frac{3\sigma}{g(\rho_l - \rho_v)}}, \tag{46}$$

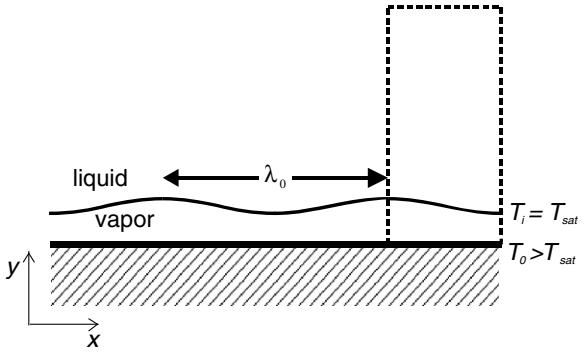

Fig. 7. Schematic of the film boiling problem.

where g is the gravitational acceleration. If initially the interface is deformed sinusoidally with this wavelength, as shown in Fig. 7, it is expected that bubbles with a pitch of λ_0 grow from the film.

The two-dimensional film boiling problem has been studied in a number of papers, among others in the works of Welch and Wilson [27], Juric and Tryggvason [12], and Gibou et al. [7]. There are no analytical solutions, so the comparison can only be done with previously obtained numerical results.

5. Numerical details

All CFD results to be reported in the following were obtained with the VOF method as implemented in the commercial finite-volume based flow solver FLUENT, versions 6.2.16 and 6.3. In combination with the other finite-volume discretized transport equations this allows solving interfacial flow problems coupled to heat transfer. The evaporation model as described in Section 3 was implemented into FLUENT via user-defined subroutines.

Concerning the VOF method, the calculations were performed with the PLIC scheme allowing reconstruction of the interface orientation within single computational cells. Youngs' method [30] generalized to unstructured meshes was used for that purpose. In 2D the method describes the interface within a computational cell as a straight line. In particular this means that it is always kept sharp and a diffusive smearing as in other versions of the VOF method is avoided. Surface tension is implemented as a body force, as proposed by Brackbill et al. [4]. Specifically, the body force is computed as

$$\mathbf{f}_{\mathrm{st}} = 2\sigma\kappa\frac{\rho_l C\nabla C + \rho_{\mathrm{v}}(1-C)\nabla C}{\rho_l + \rho_{\mathrm{v}}}, \tag{47}$$

where the curvature κ is obtained from

$$\kappa = -\nabla\frac{\mathbf{n}}{|\,\mathbf{n}\,|} \tag{48}$$

with $\mathbf{n} = \nabla C$.

For time stepping, a first-order implicit scheme

$$\phi^{n+1} = \phi^n + \Delta t F(\phi^{n+1}) \tag{49}$$

was chosen, where $F(\phi)$ denotes the right-hand side of the transport equation under study:

$$\frac{\mathrm{d}\phi}{\mathrm{d}t} = F(\phi). \tag{50}$$

In all transport equations, the discretization of the convective term was done using a third order scheme, obtained from

$$\phi_f = \vartheta\phi_{\mathrm{f,CD}} + (1-\vartheta)\phi_{\mathrm{f,SOU}}. \tag{51}$$

In this expression, ϕ_f is the value of the field quantity under study at a face of a computational cell, $\phi_{\mathrm{f,CD}}$ is the corresponding value obtained by computing the weighted average of ϕ at the centroids of the two neighboring cells (central differencing), $\phi_{\mathrm{f,SOU}}$ is the corresponding value obtained by applying a second-order upwind scheme, and ϑ is a blending factor. The contribution from the second-order upwind scheme is given by

$$\phi_{\mathrm{f,SOU}} = \phi_{\mathrm{c}} + \Delta\mathbf{s} \cdot \frac{1}{V} \sum_f \mathbf{A}_f \tilde{\phi}_f, \tag{52}$$

where ϕ_{c} is the field value at the cell centroid upstream of the corresponding face, $\Delta\mathbf{s}$ is the displacement vector from the upstream cell centroid to the face centroid, and V is the upstream cell volume. The sum extends over all faces of the upstream cell, $\mathbf{A}_f$ are the corresponding face areas, and $\tilde{\phi}_f$ are the field values at the face centers obtained by computing a weighted average of the values at the neighboring cell centroids. The diffusive term in the transport equations was always evaluated using a central-differencing scheme, i.e. the field gradient at the face centroids was determined from a weighted average of the field values at the neighboring cell centroids. With regard to the solution of the pressure-correction equation, a pressure staggering scheme was used to compute the pressure values at the cell faces from the corresponding cell centroid values. This scheme mimics the pressure evaluation on the cell faces as performed on a staggered grid [17]. For pressure-velocity coupling, the PISO scheme [11] was used.

If not stated otherwise, the following material properties of the vapor and liquid phase were assumed: $\rho_{\mathrm{v}} = 1\ \mathrm{kg/m^3}$, $\rho_l = 10^3\ \mathrm{kg/m^3}$, $\mu_{\mathrm{v}} = 10^{-2}$ mPa s, $\mu_l = 10$ mPa s, $c_{pv} = 10^3\ \mathrm{J/(kg\ K)}$, $c_{pl} = 10^3\ \mathrm{J/(kg\ K)}$, $\lambda_{\mathrm{v}} = 10^{-2}\ \mathrm{W/(m\ K)}$, $\lambda_l = 10^{-1}\ \mathrm{W/(m\ K)}$. The enthalpy of evaporation and the surface tension were chosen $h_{\mathrm{e}} = 10^6\ \mathrm{J/kg}$ and $\sigma = 10$ mN/m, respectively. No attempts were made to incorporate the effects of Laplace pressure (in the case of droplet evaporation and film boiling) on the saturation temperature. Instead, the saturation temperature was set to a fixed value of 373.15 K. In accordance with the second and third test case, the evaporation heat transfer coefficient α_{e} of Eq. (2) was used, yielding an evaporation mass flux density as given in Eq. (39). The latent heat was implemented as a source-term as defined in Eq. (25). The scale parameter $\Delta t \cdot D$ in Eq. (15) was always chosen such that the mass source-term density in each of the phases extends over 2–3 computational cells.

While all other model parameters are more or less easily accessible, the evaporation coefficient χ_{e} in the evaporation heat transfer coefficient is only known with a large degree of uncertainty even for the most common liquids. Marek and Straub [15] have analyzed the published data for the evaporation coefficient of water and found a range of roughly $10^{-3} < \chi_{\mathrm{e}} \leqslant 1$. Within that range $\sigma_{\mathrm{e}} = 1$ is the numerically most challenging value because it results in the fastest evaporation heat transfer. For this reason, an evaporation coefficient of 1 was used in all the calculations reported.

In context with the specific comparison of the CFD model results with the analytical results for the Stefan problems, a quasi 1D computational domain with only one grid cell in the direction of translational invariance was set up. The extension of this domain was chosen 1 mm and 0.5 mm for Stefan problem 1 and 2, respectively. For Stefan problem 1, the domain is bounded by two walls at $x_{\min} = 0$ and $x_{\max} = 1$ mm. For Stefan problem 2, there is one wall at $x_{\min} = 0$ and one pressure boundary at $x_{\max} = 0.5$ mm. The thermal boundary conditions are

$$T|_{x=x_{\min}} = \begin{cases} 383.15\ \mathrm{K} & \text{(Stefan 1)} \\ 573.15\ \mathrm{K} & \text{(Stefan 2)} \end{cases}, \quad T|_{x=x_{\max}} = 373.15\ \mathrm{K}, \tag{53}$$

supplemented by

$$\left.\frac{\mathrm{d}\varphi}{\mathrm{d}x}\right|_{x=x_{\min}} = \left.\frac{\mathrm{d}\varphi}{\mathrm{d}x}\right|_{x=x_{\max}} = 0, \tag{54}$$

and the impermeability condition $\mathbf{u} = 0$ for the velocity field at the wall boundaries. The zero-flux boundary condition for the scalar field, Eq. (54), is used for all boundaries of all model problems considered here. As an initial condition for the Stefan problems, the velocity was set to zero in the complete domain and the temperature equal to the saturation temperature. Furthermore, in Stefan problem 1 initially the domain was filled with liquid. In the CFD calculation this situation was approximated by initializing a vapor–liquid interface at $x = 1$ μm. In Stefan problem 2, the interface is initially located at $x = 100$ μm.

In the analytical solution of Section 4.1 the vapor–liquid interface was treated as a boundary with a prescribed temperature of T_{sat}. In order to ensure in the CFD model that the interface is at a temperature very close to T_{sat}, the thermal diffusivity of the liquid phase was increased by orders of magnitude by choosing $\rho_l = 1\ \text{kg/m}^3$ and $\lambda_l = 1\ \text{W/(m K)}$. That way it is made sure that a possible deviation of the interface temperature from the saturation temperature is rapidly diffused to the isothermal wall at $x = x_{\max}$. Furthermore, for equal densities of liquid and vapor there is no volume expansion of the system, with which impermeable walls would stand in conflict. For Stefan problem 1 (Stefan problem 2), the model domain was meshed with an equidistant grid of 1000 (500) computational cells.

The droplet evaporation problem was treated in a semicircular domain for which cylindrical symmetry was assumed. The radius of the semicircular computational domain was set to values between $r_{\max} = 3\ \mu\text{m}$ and $r_{\max} = 15\ \mu\text{m}$. Initially, 2/3 of the domain (in terms of the radial coordinate) is filled with liquid, the rest with vapor. The linear boundary serves as the symmetry axis of the 2D axisymmetric model, whereas on the semicircular boundary different boundary conditions may be defined. For the calculations reported, the following boundary conditions were chosen:

$$p|_{r=r_{\max}} = \text{const.}, \quad \left.\frac{\partial T}{\partial r}\right|_{r=r_{\max}} = 0, \quad \left.\frac{\partial \varphi}{\partial r}\right|_{r=r_{\max}} = 0, \tag{55}$$

where the polar coordinates r and θ identify a point in the semicircular domain.

As an initial condition, all velocity components were set to zero and the temperature equal to the saturation temperature. The phases were initialized such that all computational cells for which $r \leqslant b_0 = 2r_{\max}/3$ were filled with liquid, the rest with vapor. The heating rate $\dot{h}'$ is space time independent within the liquid phase where it assumes a value of $10^{13}\ \text{W/m}^3$. In the vapor phase, no heating occurs ($\dot{h}' = 0$).

In contrast to the semi-analytical model which is based on the assumption of the droplet maintaining its spherical shape during all stages of its evolution, the interface shape is explicitly computed within the CFD model, meaning that deviations from the spherical shape may occur. Such deviations are observed in the CFD calculations if the source-term of the mass conservation equation is derived from the sharply peaked function C', i.e. if no smearing is performed. In that case the interface develops recesses and bulges and loses its spherical shape. To avoid that, the scale parameter $(\Delta t D)^{1/2}$ of Eq. (15) was chosen such that the source distribution (now derived from ϕ) extends over about 4–5 computational cells (i.e. about two on each side of the interface) in each case. It is then found that the interface instability is suppressed and the droplet maintains a close-to-spherical shape. To easily accommodate the semicircular shape of the domain, an unstructured mesh of 8702 triangular cells was defined.

For the film boiling problem, different material properties were assigned in order to allow a comparison to previously published results. Specifically, the same values as in [27] were chosen, namely $\rho_{\text{v}} = 5\ \text{kg/m}^3$, $\rho_l = 200\ \text{kg/m}^3$, $\mu_{\text{v}} = 5\ \text{mPa s}$, $\mu_l = 100\ \text{mPa s}$, $c_{pv} = 200\ \text{J/(kg K)}$, $c_{pl} = 400\ \text{J/(kg K)}$, $\lambda_{\text{v}} = 1\ \text{W/(m K)}$, $\lambda_l = 40\ \text{W/(m K)}$, $h_{\text{e}} = 10^4\ \text{J/kg}$ and $\sigma = 100\ \text{mN/m}$ and $T_{\text{sat}} = 500\ \text{K}$. The gravitational acceleration was fixed to $g = 9.81\ \text{m/s}^2$. The interface temperature was set to T_{sat}, the situation considered in [27] and in virtually all other related publications, by employing the model of Eq. (2) and multiplying the evaporation heat transfer coefficient by a factor of 100.

As a model domain, the rectangular region shown in Fig. 7 was chosen. The width of the domain (x-direction) is $\lambda_0/2$, its height (y-direction) $3\lambda_0$. The two vertical boundaries are symmetry boundaries. The lower horizontal boundary is a wall with $T = T_{\text{sat}} + 5\text{K}$ and $\mathbf{u} = 0$. On the upper horizontal boundary, the pressure was set to a fixed value and the heat flux by conduction was set to zero. The initial temperature in the complete domain was set to the saturation temperature. In order to trigger a bubble formation through the Rayleigh-Taylor instability, a small perturbation of the most instable wavelength was added to a flat, horizontal interface, giving an interface shape described by

$$y_{\text{int}}(x) = y_0 + \Delta y \cos\left(\frac{2\pi x}{\lambda_0}\right), \tag{56}$$

with $y_0 = 9\lambda_0/128$ and $\Delta y = \lambda_0/160$. The computational domain was meshed with uniform Cartesian grids with a resolution of 64×192 or 100×300 in x and y direction, the first of which will be referred to as the coarse, the second one as the fine grid.

6. Results and discussion

6.1. Stefan problem 1

Results of a comparison between the analytical and the CFD model for Stefan problem 1 are presented in Fig. 8. The figure shows the interface position as a function of time for three different thermal conductivities of the vapor phase. Besides the standard case according to the specifications made previously in this section, one case with higher and one with lower conductivity was studied. The CFD results are displayed as symbols, the analytical results as lines. The curves indicate how the evaporation process is speeded up with increasing thermal conductivity of the vapor phase, whereupon excellent agreement between the analytical and the CFD results is obtained.

Another comparison is shown in Fig. 9 which displays the temperature profile in the vapor phase for different values of the parameter $c_{pv}(T_0 - T_{sat})$, abbreviated as $c_{pv}\Delta T$. Temperature is nondimensionalized by dividing through $T_0 - T_{sat}$, while nondimensionalization of distance was done by dividing through the position of the interface x_i. In this representation the analytical temperature profile is time independent and comes very close to a straight line for virtually any realistic value of $c_{pv}\Delta T$. The time independence is reproduced very well by the numerical calculations. In order to examine in detail whether the shape of the curves is reproduced by the CFD calculations, $c_{pv}\Delta T$ was increased by a factor of 200 and 2000 with respect to its default value. These two curves together with the default curve are shown in Fig. 9. Only at a 200-fold increase of $c_{pv}\Delta T$ a slight curvature of the temperature profile becomes visible which is further amplified at a 2000-fold increase. The analytical data are well reproduced by the CFD results that only show some slight deviations. A reason for the deviations could be the fact that an increase of c_{pv} enhances the imbalance of the thermal diffusion time scales between the two phases. It is well known that numerical interfacial flow computations become more challenging when the imbalance of material properties between the phases increases [18].

6.2. Stefan problem 2

Next, the numerical results for Stefan problem 2 are presented. Before this is done it is helpful to reconsider the numerical implementation of the mass source-term Eq. (21). In the region where the source-term is nonzero (the vicinity of the vapor–liquid interface) the normal stress $\mu\partial u/\partial x$ does not vanish, different from what

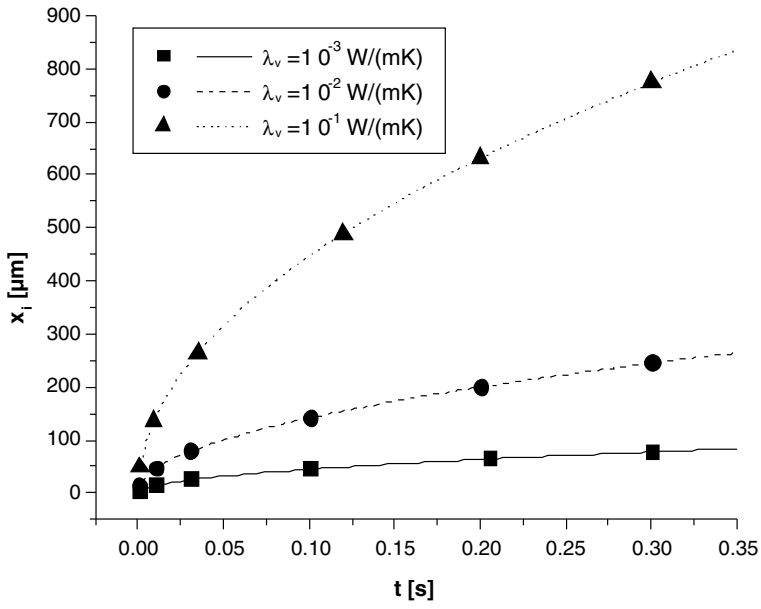

Fig. 8. Interface position as a function of time for Stefan problem 1 as obtained from the analytical (lines) and the CFD model (symbols).

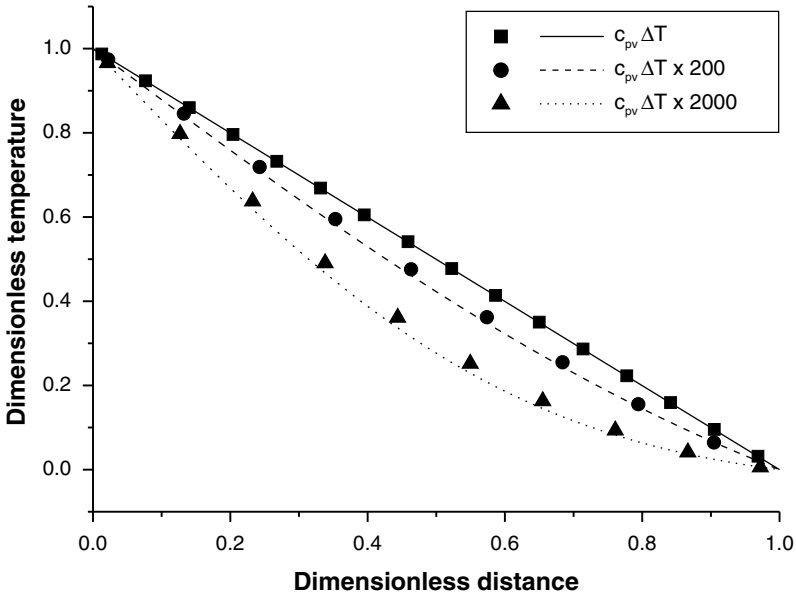

Fig. 9. Dimensionless temperature profile for Stefan problem 1 as obtained from the analytical (straight lines) and the CFD calculation (symbols).

is usually obtained for incompressible flow. In the case of constant viscosity, this stress gives rise to a force density of $\mu\partial^2 u/\partial x^2$, an artifact originating from the continuum-field representation of the mass source-term. However, it is not difficult to see that this force density does not result in a net force. Let x_1 and x_2 be two coordinates bracketing the region where the mass source-term is nonzero, either in the liquid or the vapor phase, where

$$\dot{\rho}(x_1) = \dot{\rho}(x_2) = 0. \tag{57}$$

Integration of the spurious force density results in

$$\mu \int_{x_1}^{x_2} \frac{\partial^2 u}{\partial x^2} = \mu \left(\left.\frac{\partial u}{\partial x}\right|_{x_2} - \left.\frac{\partial u}{\partial x}\right|_{x_1} \right) = 0, \tag{58}$$

due to Eq. (57). Thus, while the continuum representation of the mass source-term causes a nonvanishing dilatation stress and a corresponding force density, the net force being the integral over the force density is zero. A force density in the fluid gives rise to a pressure drop. Owing to Eq. (58) it is expected that the pressure field is locally modified in the vicinity of the vapor–liquid interface, but the net pressure drop related to the spurious force density should be zero.

These simple arguments are confirmed by the numerical results for the pressure field in the vicinity of the interface shown in Fig. 10. The diagram shows the static and dynamic pressure at two different times. Initially, the interface is located at $x = 100$ μm. After 12 ms, the static pressure (dotted line) displays a plateau in the liquid phase (left), reaches large negative values close to the interface (downward arrow), switches to large positive values on the other side of the interface (upward arrow) until it falls off with a negative slope and reaches its prescribed value zero at the outlet (not shown). At the same time, the dynamic pressure (dashed line) is zero in the liquid phase and soon reaches a plateau in the vapor phase. After 44 ms a comparable situation is found, with the difference that the static pressure (solid line) does not display a negative slope in the vapor phase.

These results are interpreted as follows. The evaporation process can be divided into two phases: (1) an initial phase where the linear temperature profile in the liquid builds up and (2) a quasi-steady-state evaporation process where the linear temperature profile is maintained and the vapor–liquid interface slowly approaches the heated wall. In phase 1 the evaporation mass flux changes rapidly as a function of time, whereas in phase 2

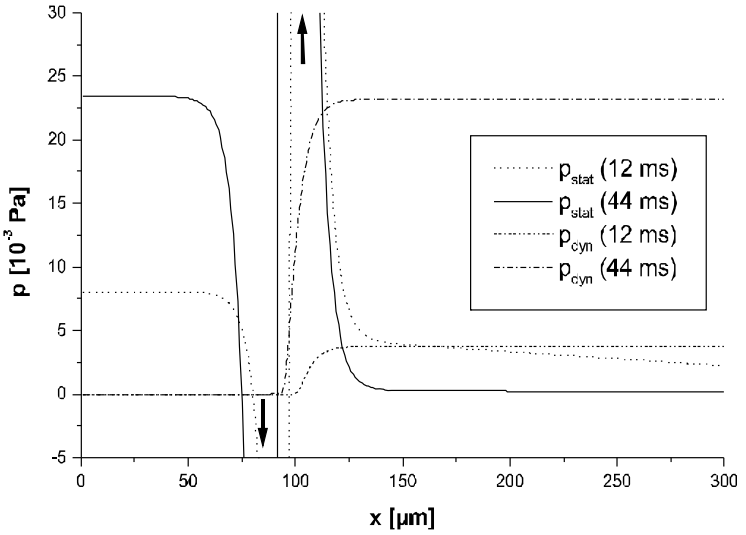

Fig. 10. CFD results for the second Stefan problem showing the static and dynamic pressure at two different times.

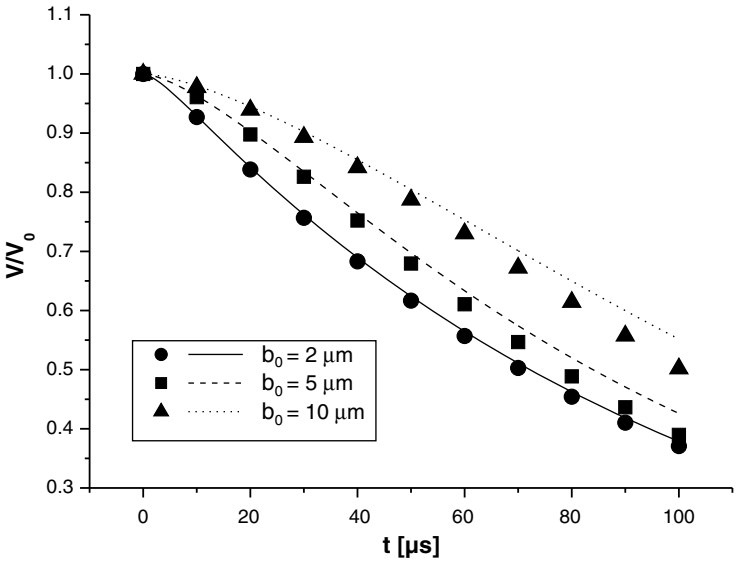

Fig. 11. Dimensionless droplet volume as a function of time for three different initial droplet radii. The semi-analyical results are shown as lines, the CFD results as symbols.

only slow changes – determined by the decreasing thermal resistance of the liquid layer – are observed. The curves in Fig. 10 at 12 ms still belong to phase 1. The slope of the static pressure in the vapor phase represents the pressure loss due to acceleration of vapor, i.e. the bulk of the vapor has not yet reached its quasi-steady-state velocity. This acceleration process has largely come to an end in phase 2, as apparent from the curves at 44 ms. In this case vapor is accelerated only in the vicinity of the interface. Both in phases 1 and 2 Eq. (37) is fulfilled, which becomes immediately apparent from the pressure curves at 44 ms. In quasi-steady-state the static (dynamic) pressure vanishes in the vapor (liquid) phase, and the plateau values of the two pressures are identical. Only in the vicinity of the interface deviations from the expected functional form due to the spurious force density related to the continuum formulation of the mass source terms are observed. It can thus be

concluded that the model reproduces the correct recoil pressure distribution, apart from artifacts occurring in the vicinity of the vapor–liquid interface.

6.3. Droplet evaporation

A comparison of the data of the semi-analytical model with the CFD results is shown in Fig. 11. The figure shows the droplet volume divided by its initial value as a function of time for three different initial droplet radii, 2 μm, 5 μm and 10 μm. The agreement between the semi-analytical and the CFD results is good for the smallest droplet, whereas some deviations are visible for the larger droplets.

To uncover the reasons for the deviations it is worthwhile to note that the CFD calculations always result in a faster shrinking of the droplet than the semi-analytical model. Thus, the CFD model predicts an enhanced heat transfer from the interior of the droplet to its surface. The reason for this heat transfer enhancement is most probably the convective heat flow due to the spurious currents induced by fluctuations of the vapor–liquid interface [18]. Spurious currents are known to be a persistent problem in interfacial flow calculations. In Fig. 12 typical velocity fields as obtained by the CFD calculation for the droplets of 2 μm and 10 μm initial diameter are displayed. The figure shows that in the case of the 2 μm droplet the maximum velocity of these fluctuations is about 4 cm/s, while for the 10 μm droplet it is about 6 cm/s. The time scale for convective heat transfer is given by

$$\tau_{\mathrm{con}} = \frac{b_0}{\bar{u}}, \tag{59}$$

where $\bar{u}$ is the average velocity of the fluctuations. By contrast, the time scale for heat transfer by conduction is

$$\tau_{\mathrm{dif}} = \frac{b_0^2}{k_l}. \tag{60}$$

Thus, $\tau_{\mathrm{dif}}/\tau_{\mathrm{con}}$ scales approximately as b_0 if $\bar{u}$ does not change significantly with the size of the droplet. The latter assertion is supported by the data shown in Fig. 12. By construction, the semi-analytical model for droplet evaporation does not contain contributions from convective fluxes. These are increasingly suppressed with decreasing b_0. Thus, this line of arguments explains why in Fig. 11 the agreement between the semi-analytical and the CFD results is improved when the droplet size decreases.

This conclusion is also supported by the data displayed on the left side of Fig. 13, showing the dimensionless volume of a droplet of 5 μm initial radius as a function of time for two different liquid thermal conductivities. The agreement between the CFD and the semi-analytical results is significantly better for the larger conductivity, indicating that as long as heat conduction dominates over convection, the evaporation model

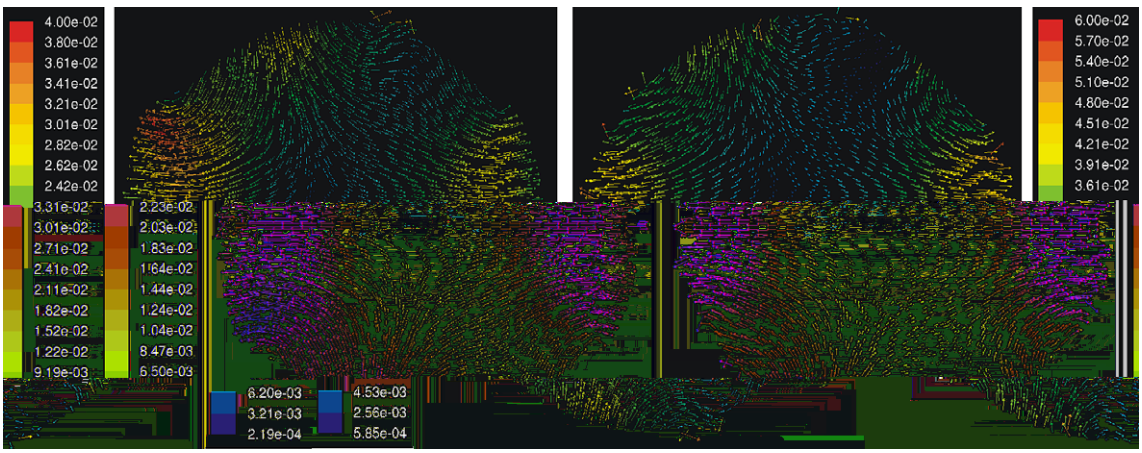

Fig. 12. Typical velocity field in an evaporating 2 μm droplet (left) and 10 μm droplet (right). The scale bars on the left and on the right indicate the velocity magnitude in m/s.

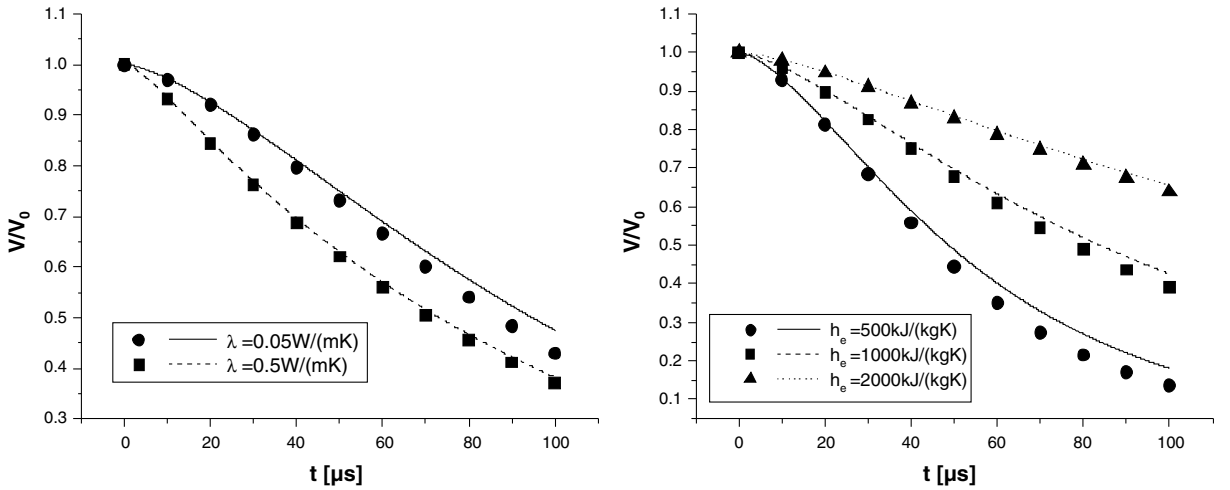

Fig. 13. Dimensionless droplet volume as a function of time for three different enthalpies of evaporation. The semi-analytical results are shown as lines, the CFD results as symbols.

in conjunction with the VOF scheme produces accurate results. The right side of Fig. 13 again shows results for a 5 μm droplet, this time with the default thermal conductivity, but with different enthalpies of evaporation. As expected, the evaporation process slows down with increasing h_e, because the higher h_e, the faster the droplet is cooled, leading to a decrease of the heat and mass fluxes. The deviations between the results of the CFD and the semi-analytical model are not significantly different in the three cases, they only appear strongest for $h_e = 500\ \mathrm{kJ/(kg\ K)}$ because they are generally enhanced in the final stages of the evaporation process where $V/V_0 \ll 1$ due to accumulation of numerical errors.

In a recent article Francois et al. [5] have analyzed in detail the origin of spurious currents within the VOF method. They compared different models for computing the curvature of the interface and implementation of surface tension. Their conclusion is that the key factor for minimizing the spurious currents is a very accurate computation of the interface curvature. A similar analysis was done by Gerlach et al. [6]. This and the

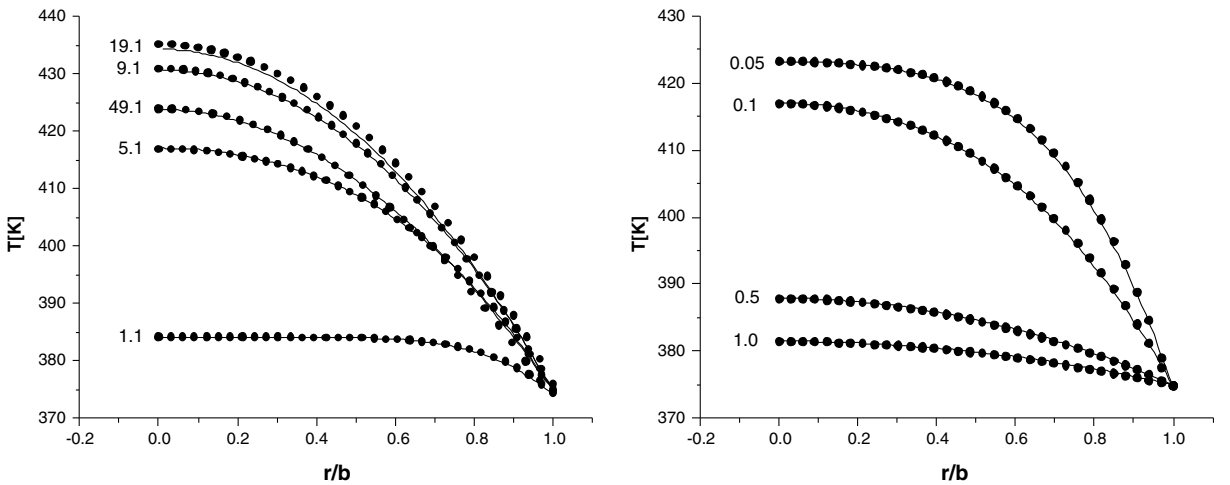

Fig. 14. Temperature profiles in the evaporating droplet as a function of the dimensionless radial coordinate. The left side shows data with the default thermal conductivity after different computational times. The time values in units of μs are assigned to the different curves. On the right side, temperature profiles obtained for a fixed time and different liquid thermal conductivities are shown, now with the conductivity values (in W/(m K)) assigned to the curves. The results of the semi-analytical model are represented as lines, those of the CFD model as symbols.

arguments presented above suggest that the shortcomings that have become apparent when examining the validation case of droplet evaporation are by no means generic to the evaporation model presented in this work but are related to the curvature term Eq. (7). Thus, the key to improvements lies in more accurately fulfilling the force balance around the interface by increasing the accuracy of the curvature computation. A quantitative evaluation of the level of spurious currents in the present computational framework was done in Appendix B.

The current model gives very accurate results if convective heat transfer due to spurious currents is negligible compared to heat conduction, as in the case of the 2 μm droplet. On the left side of Fig. 14, the radial temperature profile in the droplet is shown after different time intervals. On the right side, temperature profiles for a fixed time (5.1 μs) and different thermal conductivities are displayed. The semi-analytical results are represented as lines, the CFD results as symbols. The current droplet radius is denoted as b. The figure shows that until about 19 μs the temperature keeps increasing and is then reduced due to shrinking of the droplet. In the diagram with different thermal conductivities the curves become increasingly flat when the conductivity is increased, as expected. Overall, an excellent agreement between the semi-analytical and the CFD results is obtained.

6.4. Film boiling

Before discussing the computational results for the film boiling problem, a few remarks are appropriate. Since a 2D problem with translational invariance is considered, it cannot be expected that the results give an accurate representation of the physics of film boiling. The reason for this discrepancy lies in the inappropriate treatment of surface tension effects. A translationally invariant 2D model only accounts for the components of interface curvature lying in the computational plane, whereas the out-of-plane components are neglected. This means that surface tension driven hydrodynamic instabilities can usually not be captured in a realistic way. In particular, it is known that the Rayleigh-Plateau instability can play a role for bubble pinch off. As Gibou et al. [7] noted correctly, this instability does not show up in a translationally invariant 2D model, leading to bubbles remaining connected to the vapor film by a thin neck, clearly an unrealistic scenario. Despite of these limitations, the film boiling problem outlined in Section 4.4 has been chosen as a validation case. This choice is motivated by the fact that the test cases considered here do not serve the purpose of exploring physical evaporation problems in detail, but to provide a benchmark allowing to assess the performance of the developed numerical model. The problem qualifies as a benchmark, since it has been studied by a number of authors before and can be regarded as a standard CFD problem for evaporating flows.

The computed time evolution of the vapor–liquid interface on the fine grid is shown in Fig. 15. The top left frame corresponds to a time of 0.3532 s after initialization, while time is incremented by 0.1 s for the subsequent frames. Only one single bubble is pinched off, followed by the growth of a vapor neck finally merging with the bubble and forming a growing mushroom-shaped structure connected with the film covering the wall. A very similar scenario is found when the coarse grid is used. For the same problem, using a level-set method, Gibou et al. [7] found a quasi-steady bubble release pattern on their coarse grid, i.e. bubbles are pinched off periodically. However, they identified this scenario as a numerical artifact, since bubble pinch-off was found to be suppressed when they significantly refined their grid. Using a higher grid resolution they identified growing mushroom-shaped structures.

In this respect the results of Fig. 15 confirm the findings of Gibou et al. Also on the coarse grid only the first bubble pinches off, whereas subsequently mushroom-shaped structures are found. Apparently, in the context of the numerical model used here, also the coarse grid is fine enough to suppress the unphysical breaking of the neck, with some exceptions discussed below. These results in combination with the results of Gibou et al. suggest that the quasi-periodic film boiling process described in the paper by Welch and Wilson [27] is due to a non-converged solution and should not be interpreted as a physically realistic scenario.

It should be pointed out that, owing to the formation of thin vapor filaments, the 2D film boiling problem is numerically quite challenging. Even on the fine grid the width of the neck is resolved only by a few (about 8) computational cells. The significant fluctuations of the vapor–liquid interface discussed in Appendix B can induce a pinch-off of the neck, as becomes apparent when extending the simulations to long enough times (exceeding the time interval of Fig. 15). It is then observed that the neck breaks apart at apparently random times and positions. This happens on the fine grid and even more frequently on the coarse grid. It should,

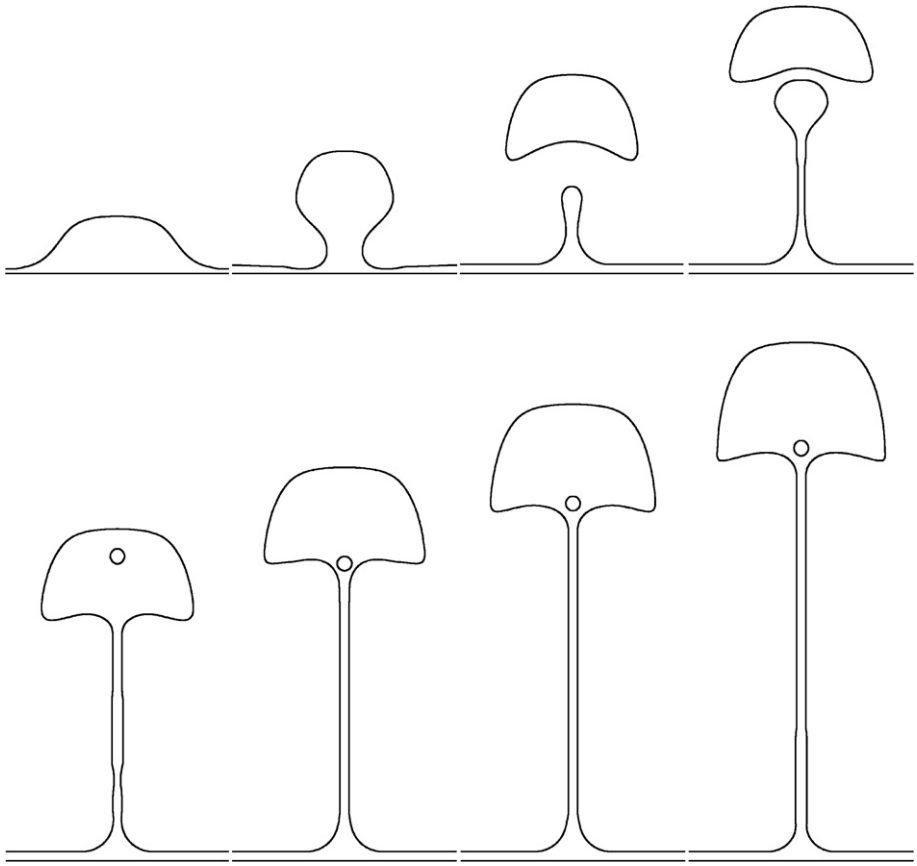

Fig. 15. The evolution of the vapor–liquid interface as computed on the fine grid. The horizontal line at the bottom of each frame is the heated wall. The circle inside the mushroom-shaped bubble is a droplet having been created via coalescence of the neck with the initial bubble.

however, be noted that such phenomena are solely due to the specific interface-capturing scheme used and have nothing to do with the evaporation model, as can be easily checked by plotting the spatial distribution of the mass source terms that are virtually zero in the region of the neck.

In order to check the grid independence of the results, the interface shapes on the coarse and the fine grids have been compared for two different stages in the bubble formation process, as shown in Fig. 16. At a comparatively early stage, there is a good agreement, as shown on the left side of the figure. Later, after the neck has been formed, the agreement deteriorates. At that stage the first bubble has already been pinched off,

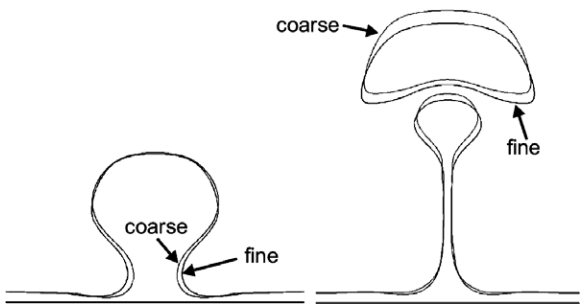

Fig. 16. Comparison of the interface shapes for two different stages of the evaporation process obtained on the coarse and on the fine grid.

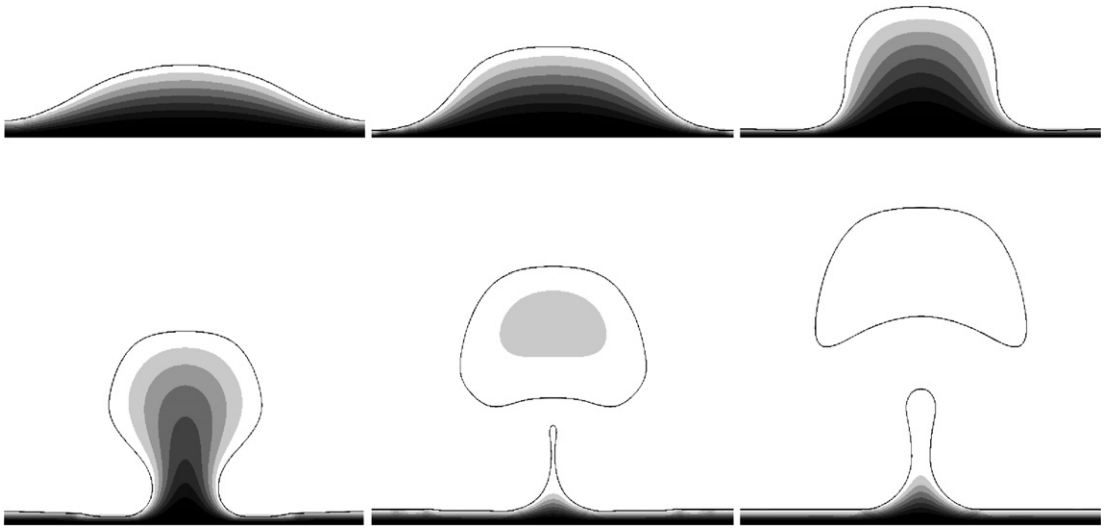

Fig. 17. The evolution of the vapor liquid interface and the temperature field for the first bubble being pinched off.

a process that is sensitive to numerical fluctuations of the interface. In principle, also the formation of the first bubble could be a numerical artifact and could be suppressed on very fine grids, an issue that could not finally be clarified with the available computational resources. However, already at this stage the qualitative behavior of the film boiling process as observed by Gibou et al. [7] could be confirmed, while a quasi-periodic bubble release process as found by Welch and Wilson [27] cannot be approved. It should be noted that, similarly as in [27], a VOF approach is used, showing that the mushroom-shaped structures are generic and not specific for the level-set method used by Gibou et al.

An aspect that does not agree with the results of Gibou et al is the shape of the bubbles. In their paper the edges of the bubbles become unstable finally resulting in a jellyfish-like shape. By contrast, the bubbles of Fig. 15 always maintain a compact shape. In this respect the results are much closer to those obtained by Welch and Wilson [27] who also observed compact bubbles without edge instabilities.

All these features concerning bubble shapes and pinch-off are related to the specific interface-tracking model and not to the evaporation model which is the focus of this work. The results of Fig. 15 demonstrate the ability of the method presented in this paper to compute evaporating flows in situations more complex than inherent in the other validation cases. The significance of evaporative mass transfer for the considered film boiling scenario can be analyzed by plotting the temperature field at different stages of the process. This is done in Fig. 17 that shows the vapor–liquid interface together with a grayscale plot of the temperature field, as obtained with the fine grid. The frame on the upper left shows the situation 0.3 s after initialization, in the subsequent frames time is incremented by 0.05 s. Ten equidistant grayscale levels are displayed, spanning the range between 505 K (wall) and 500 K (interface). From the figure it becomes apparent that initially evaporation occurs over the complete vapor–liquid interface. However, as soon as a thin neck develops, the temperature field does not significantly extend away from the wall, so that evaporation mainly occurs in the thin vapor film. Therefore, the dynamics of the mushroom-shaped bubbles shown in Fig. 15 is virtually independent of the evaporation model and its implementation.

7. Summary and conclusions

An evaporation model has been developed that by construction is largely independent of the specific realization of an interface-capturing scheme. The model was especially developed to study microscale evaporation phenomena, but is not limited to it. In context with the latter it has been shown that significant deviations of the vapor–liquid interface temperature from the saturation temperature should be expected, so that the usual assumption of an isothermal interface at saturation temperature breaks down. Correspondingly, the evapora-

tion model incorporates a physical relationship for the evaporation mass flow and allows for deviations from the saturation temperature. The model relies on a continuum-field representation of the corresponding source terms in the mass conservation equation that can be tuned by a scale parameter in such a way that numerical stability of the evaporating liquid front is achieved. The continuum-field representation should make it easy to implement the model into a number of different interface-capturing schemes irrespective of the numerical details of interface representation and propagation.

The evaporation model was implemented into the VOF scheme with piecewise linear interface construction as available within the commercial CFD code FLUENT. Calculations were performed for three analytically or semi-analytically solvable test cases, two one-dimensional Stefan problems and a free droplet evaporation problem. In addition, a two-dimensional film boiling problem was considered that has been analyzed by other authors based on the VOF and the level-set technique.

Good agreement between the numerical and the analytical results was found for the Stefan problems. With regard to the second Stefan problem, especially the recoil pressure due to the acceleration of vapor emerging from the interface to the liquid was analyzed. The mass source terms cause a local distortion of the pressure field, but nevertheless, the overall pressure distribution comes out correctly, showing that the model is capable of accounting for the recoil from vapor acceleration.

The case of droplet evaporation gives an indication of the limiting factors induced by the interface-capturing scheme. While for small droplets the agreement between the numerical and the semi-analytical results is good, some deviations were detected in cases where convective heat transfer competes with heat conduction. Spurious currents were identified as the most probable cause for this unphysical thermal convection that effects a faster droplet evaporation than in the case of pure conduction. The level of spurious currents in the employed VOF scheme was quantified in a separate effort and found to be considerable.

In the film boiling problem, a predominant evaporation mode with mushroom-shaped bubbles connected to the vapor film through a thin neck was identified. The same evaporation mode has been found by other authors [7], but stands in conflict with quasi-periodic bubble release patterns determined in earlier work [27]. The application of the model to the film boiling problem demonstrates its usefulness in more complex situations than in the other validation cases.

The most notable features of the approach presented in this paper are the possibility to implement almost arbitrary evaporation laws bearing more physical relevance than the assumption of an isothermal interface and the continuum-field representation of mass source terms that should allow including evaporation mass transfer into a number of different interface-capturing schemes such as the VOF and the level-set method.

Acknowledgment

S. Hardt acknowledges fruitful and inspiring discussions with F. Schönfeld.

Appendix A. Numerical error due to the continuum-field representation of the mass source-term

In this appendix, the scale of the numerical error due to the continuum representation of the mass source-term is computed for a spherical surface of radius b. With $a = \Delta t D$ and $k = i/a^{1/2}$ Eq. (15) is rewritten as

$$\nabla^2\varphi + k^2\varphi = -\frac{\varphi_0}{a}, \tag{61}$$

with its Green's function defined by

$$\nabla^2 g + k^2 g = -\delta \tag{62}$$

and given as

$$g(r) = \frac{\exp(ikr)}{4\pi r}. \tag{63}$$

Expanding the Green's function in spherical harmonics $Y_{lm}(\theta,\phi)$ gives

$$g(|\,\mathbf{r}-\mathbf{r}'\,|) = ik\sum_{l=0}^{\infty}\sum_{m=-l}^{l} j_l(kr_<)h_l^{(1)}(kr_>)Y_{lm}^*(\theta',\phi')Y_{lm}(\theta,\phi), \tag{64}$$

where $j_l, h_l^{(1)}$ are spherical Bessel and Hankel functions and $r_<$ ($r_>$) is the smaller (bigger) of the two values r and r'. Using a source-term of the form

$$\varphi_0(r) = \delta(r-b) \tag{65}$$

to represent the evaporation of a spherical vapor–liquid interface, expressing φ via its Green's function and making use of the orthogonality property of the spherical harmonics, it follows that

$$\varphi(r) = \frac{ikb^2}{a}\left[\theta(r-b) j_0(kb) h_0^{(1)}(kr) - \theta(b-r) j_0(kr) h_0^{(1)}(kb)\right], \tag{66}$$

with θ being the heaviside function. Using

$$j_0(kr) = \frac{\sqrt{a}}{r}\sinh\left(-\frac{r}{\sqrt{a}}\right), \quad h_0^{(1)}(kr) = -\frac{\sqrt{a}}{r}\exp\left(-\frac{r}{\sqrt{a}}\right), \tag{67}$$

results in

$$\varphi(r) = \frac{b}{r\sqrt{a}}\left[\theta(r-b)\exp\left(-\frac{r}{\sqrt{a}}\right)\sinh\left(-\frac{b}{\sqrt{a}}\right) + \theta(b-r)\exp\left(-\frac{b}{\sqrt{a}}\right)\sinh\left(-\frac{r}{\sqrt{a}}\right)\right]. \tag{68}$$

The two integrals of Eq. (29) are readily evaluated as

$$\Gamma_< = \frac{b\sqrt{a}}{2}\left[1 - \frac{b}{\sqrt{a}} + \left(1+\frac{b}{\sqrt{a}}\right)\exp\left(-\frac{2b}{\sqrt{a}}\right)\right], \quad \Gamma_> = b\sqrt{a}\left(1+\frac{b}{\sqrt{a}}\right)\sinh\left(-\frac{b}{\sqrt{a}}\right)\exp\left(-\frac{b}{\sqrt{a}}\right) \tag{69}$$

An expansion of the resulting expression for δ of Eq. (30) in powers of $a^{1/2}/b$ yields

$$\delta \approx \frac{\sqrt{a}}{b} \tag{70}$$

to leading order and apart from corrections that are exponentially small in $b/a^{1/2}$.

Appendix B. Quantification of the spurious currents

In order to quantify the level of spurious currents in the computational framework this work is based on, the same test case as in the work of Gerlach et al. [6] was considered. It consists of a fluid rod placed in a domain of square cross section. The problem is treated in 2D where the rod appears as a circle with diameter $2b = 4$ cm, while the computational domain has an extension of 6 cm × 6 cm. The domain was meshed with a uniform Cartesian grid of either 30 × 30, 60 × 60 or 120 × 120 control volumes. The rod has a density ρ_l of 1000 kg/m^3 and is placed in a background fluid with a density ρ_g of 1 kg/m^3. Since both fluids were treated as inviscid, the equilibrium state of the rod is characterized by a balance of pressure p and surface tension σ. For the latter a value of 23.61 mN/m was chosen. A time step size of $\Delta t = 10^{-5}$ s was used. Since the purpose of this test case is to quantify the level of spurious currents in the VOF model of FLUENT, no evaporation model was used. All other solver settings were kept as specified above.

As a measure for the spurious currents, the maximum of the velocity magnitude over the full model domain was computed, both after 1 time step and after 50 time steps (cf. Table 1). The results show that, independent of the grid resolution, large values for the maximum velocity are found. The values after 50 time steps are always higher than those after 1 time step and exceed the natural velocity scale of the system $(\sigma/(\rho_l \cdot b))^{1/2}$ by about two orders of magnitude. These results underpin the arguments in Section 6 and suggest that

Table 1
Maximum velocity after 1 and after 50 time steps for different grid resolutions

Grid resolution	$\lvert u_{\max,1}\rvert$ (m/s)	$\lvert u_{\max,50}\rvert$ (m/s)
30 × 30	0.05	2.16
60 × 60	0.20	2.69
120 × 120	0.04	1.52

spurious currents can significantly speed up heat and mass transfer processes across a phase boundary. Unfortunately, a direct comparison to the work of Gerlach et al. [6] is not possible, since in their paper no units were specified for the velocity values.

References

[1] F. Bazdidi-Tehrani, S. Zaman, Two-phase heat transfer on an isothermal vertical surface: a numerical simulation, Int. J. Heat Fluid Flow 23 (2002) 308–316.
[2] J.V. Beck, K.D. Cole, A. Haji-Sheikh, B. Litkouhi, Heat Conduction Using Green's Functions, Hemisphere Publishing, London, 1992.
[3] M. Bond, H. Struchtrup, Mean evaporation and condensation coefficients based on energy dependent condensation probability, Phys. Rev. E 70 (2004) 061605.
[4] J.U. Brackbill, D.B. Kothe, C. Zemach, A continuum method for modeling surface tension, J. Comput. Phys. 100 (1992) 335–354.
[5] M.M. Francois, S.J. Cummins, E.D. Dendy, D.B. Kothe, J.M. Sicilian, M.W. Williams, A balanced-force algorithm for continuous and sharp interfacial surface tension models within a volume tracking framework, J. Comput. Phys. 213 (2006) 141–173.
[6] D. Gerlach, G. Tomar, G. Biswas, F. Durst, Comparison of volume-of-fluid methods for surface-tension dominant two-phase flows, Int. J. Heat Mass Transfer 49 (2006) 740–754.
[7] F. Gibou, L. Chen, D. Nguyen, S. Banerjee, A level set based sharp interface method for the multiphase incompressible Navier–Stokes equations with phase change, J. Comput. Phys. 222 (2007) 536–555.
[8] S.C. Gupta, The Classical Stefan Problem: Basic Concepts, Modelling and Analysis, Elsevier Science, Amsterdam, 2003.
[9] H. Hertz, Ueber die Verdunstung der Fluessigkeiten, insbesondere des Quecksilbers, im luftleeren Raume, Ann. Phys. 253 (1882) 177–193.
[10] C.W. Hirt, B. Nichols, Volume of fluid (VOF) method for dynamics of free boundaries, J. Comput. Phys. 39 (1981) 201–225.
[11] R.I. Issa, Solution of the implicitly discretised fluid flow equations by operator-splitting, J. Comput. Phys. 62 (1986) 40–65.
[12] D. Juric, G. Tryggvason, Computations of boiling flows, Int. J. Multiphase Flow 24 (1998) 387–410.
[13] M. Knudsen, Die maximale Verdampfungsgeschwindigkeit des Quecksilbers, Ann. Phys. 352 (1915) 697–708.
[14] X.Y. Luo, M.J. Ni, A. Ying, M.A. Abdou, Numerical modelling for multiphase incompressible flow with phase change, Numer. Heat Transfer B 48 (2005) 425–444.
[15] R. Marek, J. Straub, Analysis of the evaporation coefficient and the condensation coefficient of water, Int. J. Heat Mass Transfer 44 (2001) 39–53.
[16] S. Osher, J.A. Sethian, Fronts propagating with curvature–dependent speed: algorithms based on Hamilton-Jacobi formulations, J. Comput. Phys. 79 (1988) 12–49.
[17] S.V. Patankar, Numerical Heat Transfer and Fluid Flow, Hemisphere Publishing, New York, 1980.
[18] R. Scardovelli, S. Zaleski, Direct numerical simulation of free-surface and interfacial flow, Annu. Rev. Fluid Mech. 31 (1999) 567–603.
[19] R.W. Schrage, A Theoretical Study of Interphase Mass Transfer, Columbia University Press, New York, 1953.
[20] G. Son, V.K. Dhir, Numerical simulation of film boiling near critical pressures with a level-set method, J. Heat Transfer 120 (1998) 183–192.
[21] G. Son, A numerical method for bubble motion with phase change, Numer. Heat Transfer B 39 (2001) 509–523.
[22] I. Tanasawa, Advances in condensation heat transfer, in: J.P. Hartnett, T.F. Irvine (Eds.), Advances in Heat Transfer, vol. 21, Academic Press, San Diego, 1991.
[23] S. Tanguy, T. Ménard, A. Berlemont, A level set method for vaporizing two-phase flows, J. Comput. Phys. 221 (2007) 837–853.
[24] G. Tomar, G. Biswas, A. Sharma, A. Agrawal, Numerical simulation of bubble growth in film boiling using a coupled level-set and volume-of-fluid method, Phys. Fluids 17 (2005) 112103.
[25] S.O. Univerdi, G. Tryggvason, A front-tracking method for viscous, incompressible, multi-fluid flows, J. Comput. Phys. 100 (1992) 25–37.
[26] P. Wayner, Intermolecular forces in phase-change heat transfer: 1998 Kern award review, AIChE J. 45 (1999) 2055–2068.
[27] S.W.J. Welch, J. Wilson, A volume of fluid based method for fluid flows with phase change, J. Comput. Phys. 160 (2000) 662–682.
[28] Y.F. Yap, J.C. Chai, K.C. Toh, T.N. Wong, Y.C. Lam, Numerical modelling of unidirectional stratified flow with and without phase change, Int. J. Heat Mass Transfer 48 (2005) 477–486.
[29] T. Ye, W. Shyy, J.N. Chung, A fixed-grid sharp interface method for bubble dynamics and phase change, J. Comput. Phys. 174 (2001) 781–815.
[30] D.L. Youngs, Time-dependent multi-material flow with large fluid distortion, in: Numerical Methods for Fluid Dynamics, Academic Press, San Diego, 1982.